Development of a Finite Element Ovine Thorax Model for use as a Pre-Test Prediction Tool in the Study of High-Rate Non-Penetrating Blunt Injuries

Juliette M. Caffrey, Patricia K. Thomas, Wade Von Kleeck III, Jeremy Schap, Matt Davis, Caitlin M. Weaver, Mike Kleinberger, F. Scott Gayzik

Abstract Personal protective equipment (PPE) is worn to prevent penetrating injuries; however, this type of insult can result in high-rate non-penetrating blunt injuries (NPBI). Fatal injuries have been observed in PPE that meet the current safety standard. This paper presents the development of an ovine thorax finite element model (FE-OTM) for use as a pretest prediction tool in early-stage evaluation of the NPBI environment. The model advances upon prior ovine models in the literature through more biofidelic modelling practices in the ribs and spine. The FE-OTM was developed from CT scans of a male 30-35 kg Katahdin sheep taken 20s post contrast. The model was simulated in 20 robustness simulations covering three impact angles (perpendicular to spine and ribs and oblique to ribs), representing the NPBI environment, all successfully terminated. The force response was in the same range of peak NPBI forces from literature. The output metrics of force, energy, impulse, and strain were analysed. Impact severity increased with impactor depth, speed, and for the normal to spine impact angle. First and 3rd principal strain were on the same order of magnitude. The applied injury criterions from literature for pulmonary contusion made a significant difference on predicted injury volume.

Keywords Back face deformation, finite element model development, high-rate non-penetrating blunt trauma, injury prevention and mitigation, ovine.

I. INTRODUCTION

Personal protective equipment (PPE) has been worn to prevent penetrating injuries; however, this can still result in high-rate non-penetrating blunt impact (NPBI) injuries with serious complications, and even death [1]. The NPBI causes motion of the chest wall, which transfers energy to the underlying bony structures and organs. While it is known that the chest wall motion affects the severity of the resulting injuries, the exact mechanism is unknown [1].

In thoracic blunt trauma, the ribs undergo a bending moment due to back face deformation of the body armour and often causes fracture to ribs in the local area of deformation [2]. The chest wall deflection also applies a shear load to the underlying tissue (lungs and heart) that can result in lacerations and contusions [1]. Additionally, the acceleration of the chest wall during impact causes pressure waves to propagate through the body. These pressure waves reflect off semi-rigid structures like bone and create complex loading and stress concentrations within the body. While these stress waves do not cause gross motion, certain areas of the body, such as the alveoli in the lungs, are susceptible to injury from the high tensile strain upon rebound from compression and will become contused [1]. Individuals who receive pulmonary lung contusions are at a higher risk for complications including pneumonia, acute respiratory distress syndrome (ARDS), and long-term respiratory disability when compared to other trauma patients [3].

To reduce the severity of high-rate NPBIs there is a need to limit the energy transferred to the body through back face deformation of PPE. Therefore, the US National Institute of Justice (NIJ) developed a safety standard for PPE design. The NIJ standard allows for a maximum deflection of 44 mm into a homogenous block of nonhardening, oil-based modelling clay [3]. However, this standard does not consider how other impact parameters effect injury risk nor provide information on what types or severity of injuries may occur [4]. Studies have shown that rib fracture and skin injury risk are related to impact velocity [5-7] and that severe pulmonary contusion can occur below 44 mm deflection [8]. Additionally, recent analysis of the 44 mm clay block criterion suggests that it corresponds to a 3.4% mortality risk [9]. Therefore, it is necessary to gain a better understanding of the mechanism causing high-rate NPBIs to develop better safety standards and PPE.

Prior work in high-rate NPBI injury mitigation has applied three different types of models: physical surrogates,

J. M. Caffrey and P. K. Thomas are PhD. Students in Biomedical Engineering, W. von Kleeck III is a Research Engineer in the Center for Injury Biomechanics, and F. S. Gayzik is an Associate Professor in the Department of Biomedical Engineering at Wake Forest University in North Carolina, USA. (Email: sgayzik@wakehealth.edu, Phone: +1(336)716-6643). J. Schap is a Biomechanical Engineer and M. Davis is VP of Technology and Development at Elemance in North Carolina, USA. C. M. Weaver and M. Kleinberger are Biomedical Engineers at DEVCOM Army Research Laboratory in Maryland.

animal models, and finite element (FE) models. There are two distinct types of physical surrogates that have been used for high-rate NPBIs. The first type is a homogenous block of nonhardening, oil-based modelling clay [10]. These blocks are inexpensive and allow for a large number of tests to be easily conducted; however, they provide no anatomical data. The only measure available from these surrogates is maximum post-test back face deformation of the PPE. The second type are physical surrogates designed to mimic the human torso such as one developed by [11-14], to study high-rate NPBIs. This model is reusable and has human–like anatomy, but its use is limited by the availability of validation data and instrumentation. Since high-rate NPBI experimental testing cannot be conducted on living human subjects, this modelling approach must be validated against post-mortem human subject (PMHS) data; however, PMHSs will not show relevant injuries like pulmonary contusion since it requires a physiological response to present [1]. Prior studies have used FE models for real event reconstruction to supplement PMHS injury predictions and inform the use of FE models for NPBI [15-18].The use of live animals allows for experimental testing and quantification of injury outcomes, from insult to injury. This creates an opportunity to observe the occurrence of injuries that cannot occur in PMHS testing. The shortcoming of this approach is that animal tests are costly, time consuming, and require additional translational study to predict injury in humans. Past studies in this area have used ovine, caprine, porcine, and canine subjects [3], [4], [14-16]. Among these species, ovine subjects have been noted as being optimal for NPBIs given the anatomical and physiological similarities between the ovine and human lung [22-24].

Finally, a computational approach using FE models can provide reproducible results at a lower cost and time per test than experimental testing and physical surrogates. Unlike physical surrogates, these models are not limited by instrumentation, as quantifiable mechanical metrics at gross and localised scales can be queried from the model. However, these models need to be validated against experimental data prior to use. Work by [11-14] developed FE models for a clay block and the human surrogate torso model. These models indicated that the NIJ standard is not sufficient to prevent injuries for higher kinetic energy impacts and also noted a lack of data on pressure and stress in organs to compare their results to [11-14]. A study by developed an ovine thorax for use in the pressure wave environment [25]. The use of an ovine subject allows for the model to be validated against experimental testing on live subjects and for the model's mechanical metrics to be correlated to injury. The drawback of this model is the lack of wide availability and simplification of key structures for the high-rate NPBIs response including a coarse mesh, ribs modelled as a single layer of shell elements, lungs meshed node to node with surrounding soft tissue, and the spine as a rigid column.

This paper presents the development of an ovine thorax explicit time integration FE model for the high-rate NPBI environment. The model offers an advancement upon prior models found in the literature through more biofidelic modelling practices in the ribs and spine. It is intended to serve as a pre-test prediction tool to assist in determining impact parameters that have the greatest effect on severity. Beyond the development of the model, we explored the role of impact angle and its effect on post impact mechanical loading severity.

II. METHODS

Model Development

Prospective medical images of an ovine specimen (male, Katahdin, 30-35 kg) were used to the develop the model. Image acquisition methods can be found in the literature [26]. The reference images used for the Ovine Thorax Model (OTM) development were 20s post contrast computed tomography (CT) scans (Fig 1). Both the soft tissue and bone reconstructions were used for segmentation, which due to lack of automated segmentation methods for ovine scans, were completed manually.

Fig 1: Sagittal view of the 20s post contrast scan using a lumbar filter.

The segmentation for this model focused on the thoracic region of the subject and included sternebrae 1 – 6, right and left calcified cartilage 1 -10, right and left scapula, right and left ribs 1 – 13, vertebral bodies C5 – L4, lungs, airway, heart, vasculature, right and left kidneys, spleen, liver, rumen, and outer surface. The segmentation workflow is shown in Fig 2. First a mask of the part in question was generated in Mimics v.23 (Materialise, Leuven, Belgium) using the semi-automatic dynamic region function or the fully automatic threshold function followed by manual editing using the multi slice edit tool. The masks were then converted into polygonal surfaces and post processed through automated smoothing functions in Geomagic Studio v2014 (3D Systems, Rock Hill, SC). Followed by manual refinement of the contour edges of the polygonal surface in Mimics, to ensure all the key detail of structures was captured. Afterwards the polygonal surface was imported into Geomagic Studio for manual smoothing. Finally, the polygonal surface was compared against the reference image to confirm agreement.

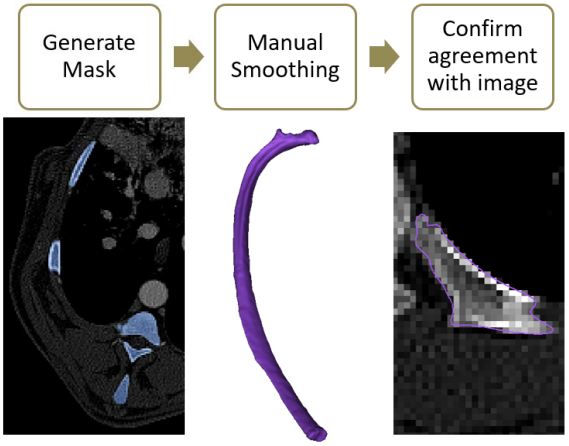

Fig 2: The segmentation workflow: mask generation, manual smoothing, and confirmation of agreement with the medical image.

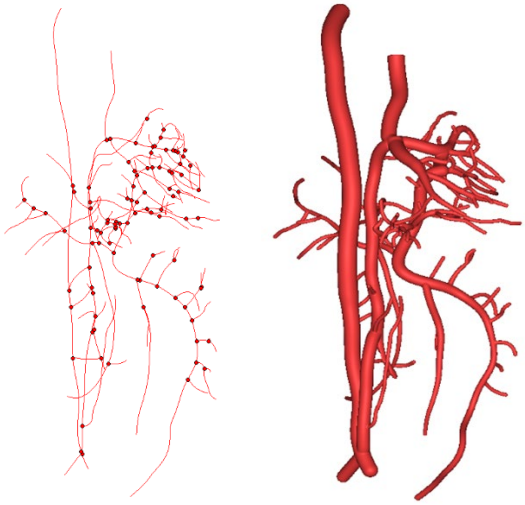

Fig 3: Left: The centerline bifurcation tree of the abdominal vasculature. Right: The abdominal vasculature generated from the bifurcation tree.

The segmentation process used for the vasculature is shown in Fig 3. During this process arterial and venous vasculature were not distinguished from one another and were treated as one part. After the mask of the vasculature was created, a centreline was fit to each vessel using Mimics. Then the centreline bifurcation tree was used to generate vessels of set diameter based on the bifurcation level using 3-matic v.16 (Materialise, Leuven, Belgium). Starting from the heart, the initial branch size was the ascending aorta 17 mm, descending aorta 15 mm, ascending vena cava 12 mm, and descending vena cava 13 mm. After which the first bifurcation was 10 mm, the second bifurcation was 5 mm, and the third bifurcation was 3 mm. Measurement was taken in the reference image throughout the process to ensure appropriate sizing.

The mesh development was completed using ANSA v 22.0 (Beta CAE Systems, Farmington Hills, MI). The mesh development had two main thrusts. The first was the application of mesh to structures that had been segmented and the second was the development of structures that did not have segmentation (due to their lack of visibility in the CT scan). During the first phase of meshing, the target mesh size for cortical bone (1 mm) was selected based on the general material properties of bone ($E \approx 4$ GPa, $\nu = 0.35$, $\rho \approx 1.06e\text{-}6$ kg/mm3) for a timestep of about 0.4 ms. There were four types of structures developed during the second thrust: intervertebral disks (IVD), intercostal muscle (ICM), the diaphragm, and a portion of soft tissue envelope for impacting. The intervertebral discs (IVDs) were formed by creating a shell bridge mesh between two adjacent vertebral bodies. The intercostal muscles (ICM) were created by defining a volume in the space between adjacent ribs, costal cartilage, and sternebrae and then filling the volume with a solid mesh. The diaphragm was created by forming a shell projection of the bottom surface of the lungs, offsetting it, bridging the mesh to the chest wall, and using Boolean operations to cut out sections of the diaphragm where the vena cava and aorta passed through. The surrounding section of diaphragm was then remeshed node to node with the vasculature. A section of soft tissue envelope, e.g., flesh, was developed around the area of impact on the model (left side, rib level 3 – 13) by offsetting the surface of the model to represent the thickness seen in the CT images (15 mm). The element quality criteria, shell thickness, and target mesh size for each type of structure can be found in Appendix A. The element criteria fall into two categories, based on the percentage of elements that must meet the criteria: 100% targets (Jacobian and

tetrahedral (tet) collapse, meaning that all elements must meet or exceed the targets in Appendix A) and 99% targets, meaning that 99% of all elements must meet the listed targets.

The model assembly was completed using LS-PrePost v4.7 (Ansys, Canonsburg, PA) and can be seen in Fig 4. All the constitutive material models used were adapted from literature and can be found in Table 1. The thorax explicitly represented with elements had a mass of 9.54 kg after applying the material models. To account for the total mass of the subject, mass nodes were added to represent the remaining portions of the body: 3.52 kg for the head and neck, 3.46 kg for the left front leg, 3.46 kg for the right front leg, and 11.21 kg for the pelvic region and rear legs [27]. The mass nodes were located approximately at the centre of mass of the represented body region and constrained to move with the closet vertebral body, resulting in a total model mass of 31.2 kg, which falls within the mass range for the scanned animal from the reference images. All parts in the model were included in an automatic single surface contact, except for solid meshes that were encapsulated in shell parts representing parenchymal surfaces. The flesh to chest wall interface employed a tied shell edge to surface contact. While the lungs to chest wall, lungs to diaphragm, rumen to diaphragm, liver to diaphragm, spleen to diaphragm, liver to rumen, and spleen to rumen interfaces all used automatic one-way surface to surface tied sliding contacts.

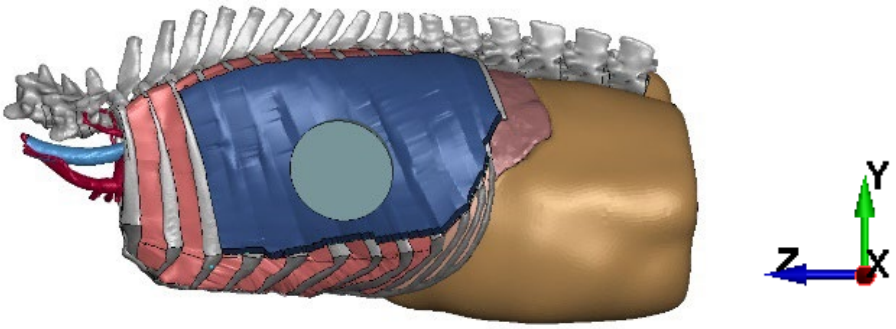

Fig 4: Picture of the full meshed model, showing where the impactor was located with respect to the model.

TABLE 1
CONSTITUTIVE MATERIAL MODELS USED AND THEIR REFERENCES

Material Model	Part	Reference
Elastic	Trabecular Bone	[28]
	Cartilage	[28]
	Intervertebral Discs	[29]
	Diaphragm	[30]
	Heart	[31]
Simplified Rubber/Foam	Intercostal Muscle	[32]
*Based on Ogden Rubber	Airway	[33]
	Lung	[34]
	Diaphragm	[30]
	Adipose	[35]
	Skin	[36-38]
	Vasculature	[39]
Rigid	Vertebrae	[28]
Fluid Elastic	Liver	[40]
	Rumen	[40]
	Abdomen (other)	Water
General Viscoelastic	Outer Flesh	[28]
Ogden Rubber	Liver Parenchyma	[41]
Piecewise Linear Elastic	Cortical Bone	[28]

Joints between adjacent vertebral bodies were constructed by defining a local coordinate system at the centre of each intervertebral disc such that positive local x was anterior, y was to the right, and z was inferior. At the origin of each local coordinate system a 0-length beam was defined as nonlinear, with 6 degrees of freedom (DOF) using joint stiffness curves from *[42]*, and with one node constrained to move with each of the adjacent vertebral bodies. Through a similar method, the joints between the costovertebral junctions were defined as spherical joints by using a constrained nodal rigid body (CNRB) of the rib head. Two congruent local coordinate

systems were developed such that the origin was at the centre of mass of the CNRB, and the positive local x was the long axis of the rib, y was normal to the anterior side of the rib, and z was superior. One coordinate system was constrained to the rib and the other to the vertebral body. The joint stiffness was based on curves from *[43]*.

Impacts Setup and Calculations:

The simulations were run in LS-Dyna's (Ansys, Canonsburg, PA) explicit solver R9.3.1 using an Intel-MPI 2018 Xeon64 and Linux CentOS6.5 um with double precision using 45 cores with 16GB of memory per core. No additional constraints were placed upon the model. The impactor used was made of aluminum with a weight of 170 g and a diameter of 80 mm in a hemispherical shape and was designed to model the general behavior of dynamic backface deformation of PPE [4-5], [44-46]. The impactor was placed at three different impact angles normal to spine, normal to ribs, and oblique to ribs. All impact positions were the same height in the y-direction and at the same rib level in the model (8^{th} rib), the only difference was the angle of the impactor about the y-axis. A total of 18 different robustness simulations were run at two different impact angles (normal to spine and normal to ribs, Fig 5), two different impact velocities (40 m/s and 70 m/s), and five different impact depths (20, 25, 30, 40, and 55 mm). For the *normal to spine* case, the line of action of the impactor was situated normal to a line connecting the spinous processes of the vertebral bodies of the thoracic spine. The *normal to rib* impact was aligned such that the line of action of the impactor was situated normal to the surface of the ribs (~18 degrees from the spine normal). Note that the 55 mm depth was run only for the 40 m/s impact depth. An additional 2 simulations were run at an oblique angle to the ribs (~-18 from the spine normal) at the impact conditions of 40 m/s 55mm and 70 m/s 40 mm for a preliminary look at angle sensitivity. The impactor's standoff was 5 mm away from the model and the displacement was prescribed based on preliminary data (Appendix B).

The outputs extracted from the model were force at the impactor to flesh contact, displacement of the flesh node closest to the initial point of contact with the impactor, and strains in the impacted lung. The force measurement was used to calculate energy and impulse by integrating it over the spatial and time domains, respectively. The strain in the impacted lung was used to run a cumulative normalised volume analysis, where the volume of every element in the impacted lung was normalised with respect to the total volume of the impacted lung and paired with the maximum strain that occurred in that element over the course of the impact. Then the elements were ordered from greatest strain to lowest strain. Finally, the cumulative volume was calculated by summing an element's normalised volume with the volume of all elements before it in the order. This represents the percentage of the impacted lung volume that experienced at least ε¬min,v strain. The cumulative volume analysis was also examined for a reduced portion of the lung which included a cylindrical volume directly beneath the impactor, 60 mm in diameter, that goes through the full thickness of the lung and only contains solid lung elements. This volume was then further broken down into three regions: proximal (30 mm radius), middle (60 mm radius), and deep (90 mm radius) using concentric spheres to compare the strain time history in the lung during the impact.

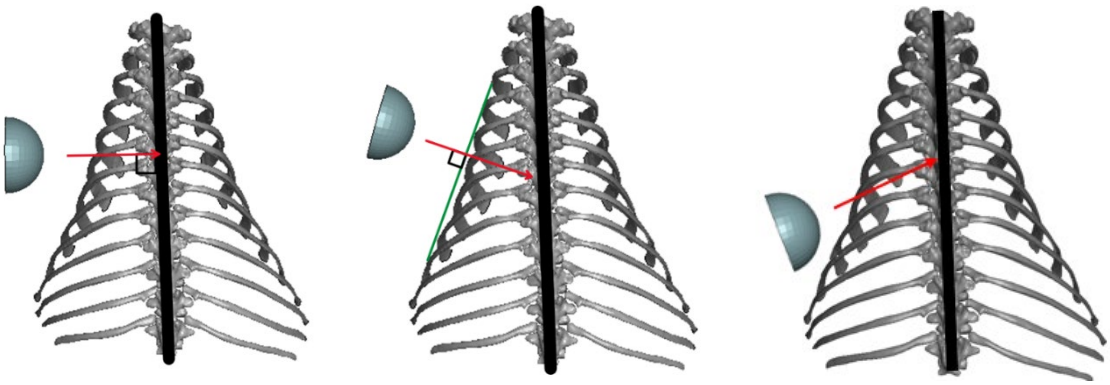

Fig. 5. The impactor positioning for the normal to spine, normal to ribs, and oblique to ribs impact positions.

III. RESULTS

Model Development:

The meshed model includes 3.2 million solid elements and 486 thousand shell elements. No elements failed the Jacobian or tetrahedral collapse criteria. For the 99% targets: 0.12% of the elements failed skewness, 0.08% failed warping, and 0.03% failed aspect ratio. The model includes 10 contacts: 1 automatic single surface, 1 tied

shell edge to surface, and 8 automatic one way surface to surface contacts. The result was about 1.5 hours of run time for 10 ms of simulation time, or a run time ratio of 9 minutes per 1 ms of simulation time with a minimum timestep of 3.33e-4 ms, which was close to the designed time step of 0.4 microseconds.

Impacts

All 20 of the simulated impacts normally terminated with less than 10% hourglass energy. The maximum force and peak energy of each simulation can be seen in Figure 6. The trends in Figure 6 show that both the peak force and energy increase with impactor depth, impactor speed, and for the normal to spine impact angles. However, there is a decrease in peak force going from the 40 mm to the 55 mm maximum impactor depth. To further explore this decrease in peak force the time history traces for force and impulse are shown in Figure 7. These plots show that while the 55 mm impact depth experiences a lower peak force, the force has a longer duration and results in a higher impulse than the impacts at lower impact depths.

An example of the strain time history response of the lung tissue is shown in Figure 8. This response is for the 40 m/s, 55 mm normal to spine impact, which was one of the most severe impacts run. The strain shown in the figure is of the reduced lung volume that was broken down into the proximal, middle, and deep regions. From these exemplar strain time history traces, the 1st and 3rd principal strains are on the same order of magnitude, that strain is highest in the proximal region, and that there is a slight delay in strain response in the deeper regions. To further analyse the strain response in the lung, a cumulative normalised volume analysis of the 1st principal strain was conducted on the entire volume of the impacted lung. The results of this analysis can be seen in Fig 9. All simulations experienced peak 1st principal strains upwards of 100% in small portions of the lung and peak strains upwards of 10% in the entire lung. The predicted volume of contused lung using a liberal injury criterion of 15.4% strain and a conservative injury criterion of 52.5% is shown in Fig 10 [47-48]. Based on the 15.4% injury criterion all simulations predict the occurrence of contusion in at least 40% of the impacted lung and that impacts depths greater than 40 mm result in near 100% contusion of the impacted lung. Using the 52.5% injury criterion all simulations predict that the impacted lung will be up to 16% contused. Trends show that impact severity is seen to increase with impactor depth, impact speed, and for the normal to spine impact angle.

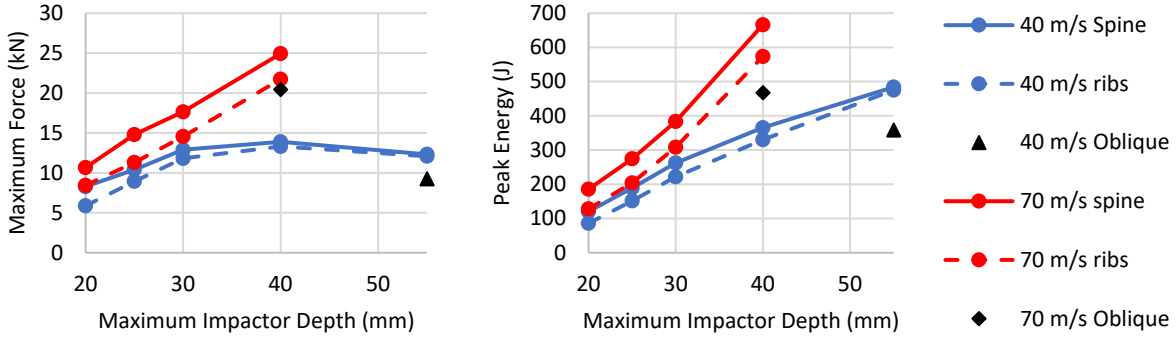

Fig. 6. The peak force and energy of each impact per the maximum impactor depth of said impact.

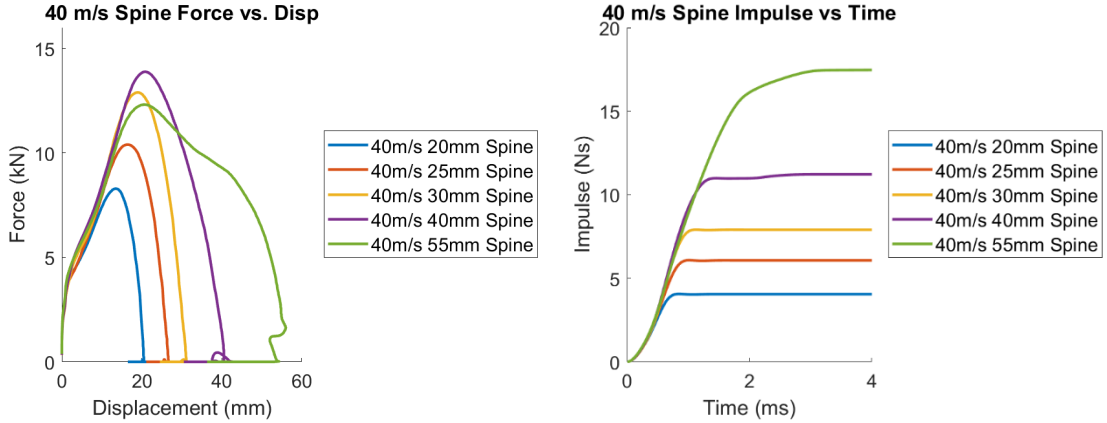

Fig. 7. Exemplar force and impulse time history traces for the 40 m/s normal to spine impact angles.

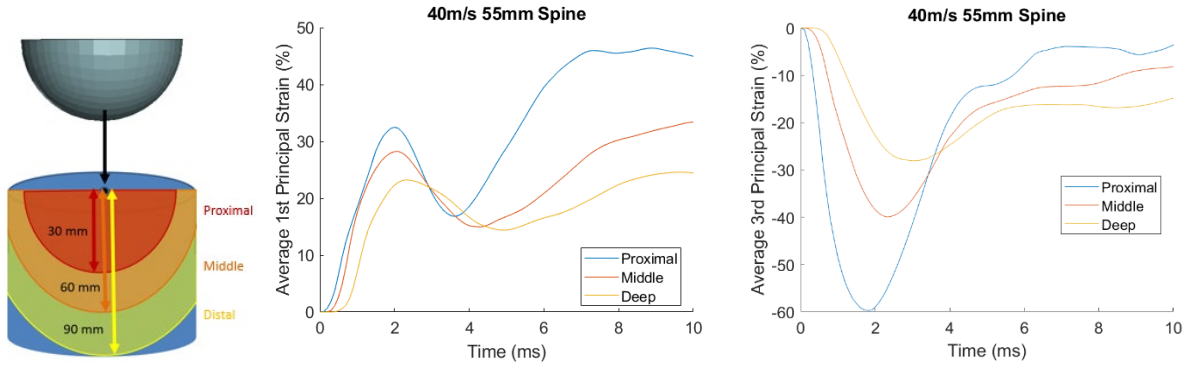

Fig. 8. Left: The three regions (proximal, middle, and deep) of lung directly under the impactor. Middle and Right: The time history of 1st and 3rd principal strain in the three regions of lung for the 40 m/s 55mm.

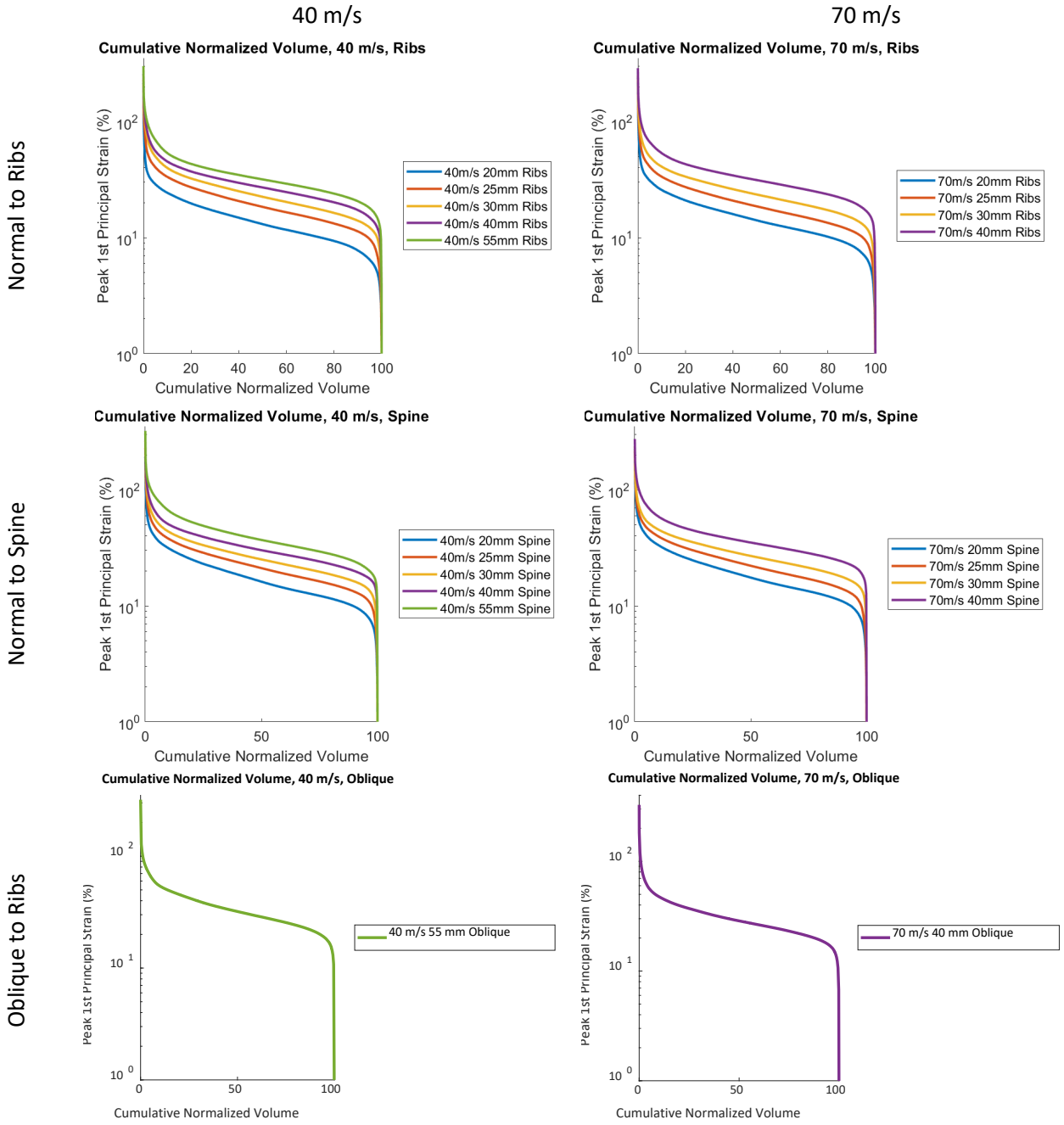

Fig. 9. The cumulative normalised total impacted lung volume of 1st principal strain for each simulation.

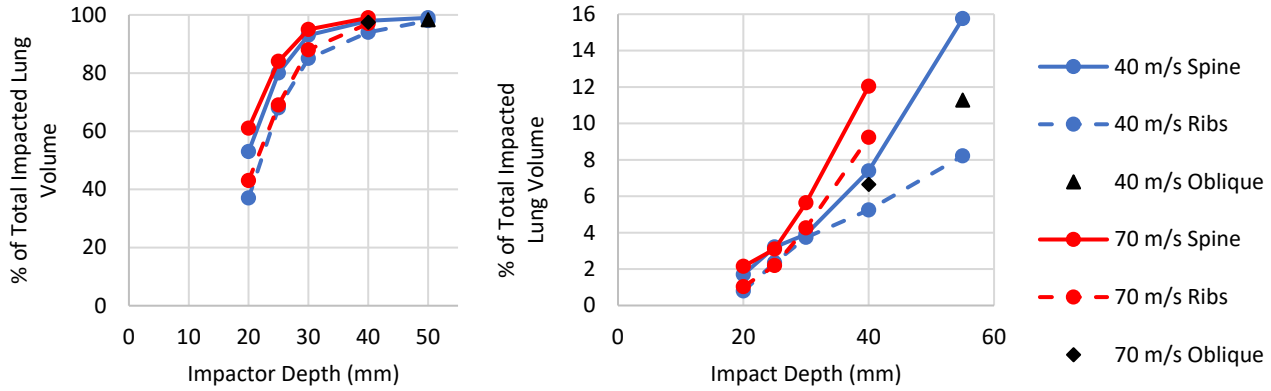

Fig. 10. Left: Shows what percentage of the total impacted lung volume would be damaged for an injury criterion of 15.4% 1st principal strain. Right: Shows what percentage of the total impacted lung volume would be damaged for an injury criterion of 52.5% 1st principal strain.

IV. DISCUSSION

This model improves upon those currently available in literature by implementing a finer mesh, detailed joints between the vertebral bodies and ribs, and improved contact between the lungs and chest wall. The Gibbons model used 85,000 elements, one-layer shell ribs, a rigid spinal column, and a node-to-node mesh between the lungs and surrounding tissue. In comparison, this new model has about 3.5 million elements, anatomically accurate rib geometry, tied sliding contacts between the lungs and chest wall/diaphragm, and intervertebral joints.

Some simplifications were made to the model for general improvement purposes. First, the legs, head, and pelvis were included as point masses in the model. This simplification means that a detailed mesh of the appendages and head did not have to be created which significantly reduces file size and computational time. This simplification is effective for thorax applications of the model but does limit the application of the model from studying trauma to the head or limbs. The large surface area of the vasculature made it infeasible to use the manual conditioning method applied to the other structures. However, it was deemed important to maintain the vasculature anatomy through the segmentation process due to the potential influence of the change in material properties on pressure wave propagation through the body. Therefore, a separate conditioning method for vasculature was developed. This method allowed for the vasculature tethers to organs and the approximate volume of vasculature greater than 3 mm in diameter to be maintained.

The current study focuses on the development and robustness of the FE-OTM model. Direct validation was not considered at this time however some inferences to other literature sources can be made on the response. A study by [46] measured the sternal contact force behind hard body armour for 7.62 mm projectile impacts at 670 – 800 m/s into PMHS specimens. The impacts resulted in about 30 – 40 mm of backface deformation and 15 to 25 kN of maximum sternal impact force. This is the same range of maximum force observed in the 70 m/s impacts with maximum impactor depths of 30 – 40 mm. This is not a direct comparison to the current study, which impacted the lateral side of sheep ribs using a NPBI representative impactor; however, the comparison confirms that the impact depths and resulting forces are within the range of experimentally measured values for NPBI. For all measured parameters the normal to spine impact angle was found to be more severe than the normal to ribs impact angle with the increase in severity becoming greater as impact velocity increases. The oblique to ribs impact angle was only studied for the most severe cases (40 m/s 55 mm and 70 m/s 40 mm) and was found to have a lower force and energy response than both the normal to ribs and normal to spine impact angles. Indicating that the effects of impact angle would be worth further investigation in future studies.

The lung strain response showed that the 1st and 3rd principal strains are on the same order of magnitude for this impact, which is supported by work done by [47]. The modeled lung is nearly incompressible; therefore, deformation occurs in the off-axis directions when subjected to compression. The implication of this is that for this impact the tissue is both compressed (normal to the impact) and stretched (perpendicular to the impact). If a more compressible lung material had been used, there would have been an increased amount of compressive strain (3rd principal strain) and a decrease in tensile strain (1st principal strain). [38] has shown that pulmonary contusion is most likely tied to overstretching of lung parenchyma. This typically results from the rebound after

compressing air filled lungs, but here we see that there is also likely gross tension of the lung tissue from the insult even in the absence of extensive rebounding. Together this indicates an elevated likelihood of contusions and tissue damage but is supported by prior work [34, 47].

The lung strain analysis revealed that the entire lung experienced at least 10% strain in every simulation. 1st principal strain-based lung injury threshold values in literature range from 15.4 – 52.5% [48-49]. Preliminary injury comparisons in this study were made using the liberal end of the range, 15.4% strain, which predicted that at least 40% of the impacted lung volume is contused in every simulation [48]. An additional comparison was made to a conservative injury threshold value of 52.5% strain which predicted up to 16% of the impacted lung volume is contused [49]. Using a liberal injury criterion of 15.4% strain, no significant difference was seen in predicted injury volume at higher depths. On the other hand, using a more conservative injury criterion of 52.5% not only was there a significant decrease in the predicted injury volume but also a differentiation between impact angles. The percent of total lung contused can be estimated dividing the percentage of the impacted lung by 2, greater than 20 percent of the total lung volume would indicate a severe injury at risk for complications including ARDS and pneumonia [3], [51-53]. The impact severity predicted by the strain-based injury criterion proved to be more of a function of depth than speed. The constitutive lung material model used was a simplified rubber with an Ogden fit, which does not include viscoelasticity. Therefore, increased impact speed would not directly affect the strain experienced by the lung. This injury prediction could be improved by developing a constitutive ovine lung material model that includes viscoelasticity. Since this model has not yet been validated against experimental data, further experimental testing is required to determine the accuracy of this model. Additionally, the development ovine tissue specific injury threshold values using the FE-OTM in conjunction with experimental outcome data after validation would further improve injury predictions. However, the level of severity between impact conditions can still be compared which is beneficial for pretest predictions and determining which variables are worth further investigation.

This model will be useful in determining the level of influence an impact parameter (impact speed, impact angle, impact depth, impactor shape, etc.) has on the resulting severity of the impact. This allows investigators to narrow down the number of experimental test subjects required for the investigation into high-rate NPBI injuries and mitigation. The next steps for this work include updating the material models to represent ovine tissue and to validate the model. After validation future work with this model will be to use it to investigate finite element analysis based injury criteria for pulmonary contusion, rib fracture, and bruising.

V. CONCLUSION

A FE ovine thorax model was developed for use as a pretest tool in the high-rate NPBI testing environment. The model was developed from CT scans of a male Katahdin sheep taken 20s post contrast. All segmentation was compared with the medical images to ensure proper agreement. The developed mesh met the desired element quality standards. All the material models used are available in literature. After development the model was put through a series of 20 robustness simulations which all successfully terminated.

This study sought to determine how impact angle affected severity by investigating a normal to ribs, a normal to spine, and an oblique to rib impact angles. These three impact angles were studied in conjunction with impact speed and impact depth over 20 different simulations. The force response was found to be within the same range of peak high-rate NPBI forces found in literature [37]. The output metrics of force, energy, impulse, and strain were analysed. It was found that for every output metric analysed the normal to spine impact angle was most severe. It was also found that impact severity increases with impactor depth and impactor speed. Additionally, 1^{st} and 3^{rd} principal strain were observed to be on the same order of magnitude and that strain was highest in the region proximal to the impactor. The applied injury criterions from literature for pulmonary contusion were found to make a significant difference on predicted injury volume.

Data Availability Statement The OTM presented in this work is available for controlled download by Wake Forest's Center for Injury Biomechanics for use in future biomechanical studies through https://redcap.link/FE-OTM. The constitutive material models in the OTM are comprised solely of material models available in the published literature.

VI. ACKNOWLEDGEMENTS

This work was funded by the U.S. Army DEVCOM ARL under BAA #W911NF2120034. We gratefully recognize the guidance provided by Dr. Alan Goertz (DEVCOM Army Research Laboratory, Maryland) and James Gaewsky (Elemance, North Carolina).

VII. REFERENCES

[1] Cannon, L. (2001) Behind Armour Blunt Trauma - an emerging problem. BMJ Mil. Health, **147**(1):87-96.
[2] Prat, N., Rongieras, F., Sarron, J.C., Miras, A., and Voiglio, E. (2012) Contemporary body armor: technical data, injuries, and limits. Eur. J. Trauma Emerg. Surg, **38**(2):95-105.
[3] Cohn, S. M. and DuBose, J. J. (2010) Pulmonary Contusion: An Update on Recent Advances in Clinical Management. World J. Surg., **34**(8):1959-1970.
[4] Hanlon, E. and Gillich, P. (2012) Origin of the 44-mm Behind-Armor Blunt Trauma Standard. Mil. Med., **177**(3):333-339.
[5] Pageau, G., Ltd, C., Ouellet, S., and Bouamoul, A. (2022) Behind Armor Blunt Trauma Injuries Assessment with Clay Backing. IRCOBI, 477-478.
[6] Arborelius, U.P., Rocksén, D., Gustavsson, J., and Günther, M. (2021) Pulmonary hypoxia and venous admixture correlate linearly to the kinetic energy from porcine high velocity projectile behind armor blunt trauma. Exp. Lung Res. **47**(7):323-333.
[7] Shedd, D.F., *et al.* (2022) The Risk of Skin Injury Caused by High-Rate Blunt Impacts to the Human Thorax. Hum. Factors Mech. Eng. Def. Saf. **6**(1):5.
[8] Sondén, A. *et al.* (2009) Trauma Attenuating Backing Improves Protection Against Behind Armor Blunt Trauma. J. Trauma Acute Care Surg. **67**(6):1191-1199.
[9] Yoganandan, N. *et al.* (2023) A Novel Paradigm to Develop Regional Thoracoabdominal Criteria for Behind Armor Blunt Trauma Based on Original Data. Mil. Med. **188**(6):598–605.
[10] "Ballistic Resistance of Personal Body Armor, NIJ Standard-0101.04," https://nij.ojp.gov/library/publications/ballistic-resistance-personal-body-armor-nij-standard-010104. [Jun. 12, 2022]
[11] Roberts, J.C. *et al.* (2007) Computational and experimental models of the human torso for non-penetrating ballistic impact. J. Biomech, **40**(1):125-136.
[12] Roberts, J.C., Ward, E.E., Merkle, A.C., and O'Connor, J.V. (2007) Assessing behind armor blunt trauma in accordance with the National Institute of Justice Standard for Personal Body Armor Protection using finite element modeling. J. Trauma, **62**(5):1555-1561.
[13] Roberts, J.C., O'Connor, J.V., and Ward, E.E. (2005) Modeling the Effect of Nonpenetrating Ballistic Impact as a Means of Detecting Behind-Armor Blunt Trauma. J. Trauma Acute Care Surg., **58**(6):1241-1251.
[14] Merkle, A.C., Ward, E.E., O'Connor, J.V., and Roberts, J.C. (2008) Assessing Behind Armor Blunt Trauma (BABT) Under NIJ Standard-0101.04 Conditions Using Human Torso Models. J. Trauma Acute Care Surg., **64**(6):1555-1561.
[15] Cronin, D.S. (201) Application of a Detailed Thorax Model to Investigate Behind Armour Blunt Trauma. IRCOBI, **12**(92):873.
[16] Cronin, D.S. (2015) Investigation of Lung Response Resulting from Behind Armour Blunt Trauma Impact Scenarios. IRCOBI, **15**(78):722-723.
[17] Cronin, D.S., *et al.* (2018) Reconstruction of Behind Armour Blunt Trauma Impact Scenarios for Soft Armour Using a Detailed Thorax Model. IRCOBI. **18**(109):752-753.
[18] Bustamante, M. *et al.* (2019). Shell Plate Method of Reconstructing Behind Armour Blunt Trauma Impact Scenarios for Soft Armour Using a Detailed Thorax Model. *IRCOBI*, **19**(103):689-691.
[19] Liu, B., Wang, Z., Leng, H., Yang, Z., and Li, X. (1996) Studies on the mechanisms of stress wave propagation in the chest subjected to impact and lung injuries. J. Trauma, **40**(3):S53-55.
[20] Judge, E.P., Hughes, J.M.L., Egan, J.J., Maguire, M., Molloy, E.L., and O'Dea, S. Anatomy and Bronchoscopy of the Porcine Lung. A Model for Translational Respiratory Medicine. Am. J. Respir. Cell Mol. Biol. **51**(3):334-343.
[21] Lum, H. and Mitzner, W. (1987) A species comparison of alveolar size and surface forces. J. Appl. Physiol., **62**(5):1865-1871.
[22] Van Der Velden, J. and Snibson, K.J. Airway disease: The use of large animal models for drug discovery - ScienceDirect. Pilm. Pharmacol. Ther., **24**(5):525-532.
[23] Gray. M.E. *et al.* (2019) Ovine Pulmonary Adenocarcinoma: A Unique Model to Improve Lung Cancer Research. Front. Oncol., **9**(335):1-11.
[24] Albertine, K.H. (2015) Utility of large-animal models of BPD: chronically ventilated preterm lambs. Am. J. Physiol. - Lung Cell. Mol. Physiol., **308**(10)L983-L1001.
[25] Gibbons, M.M., Dang, X., Adkins, M., Powell, B., and Chan, P. (2015) Finite Element Modeling of Blast Lung Injury in Sheep. *J. Biomech. Eng.,* **137**(4).
[26] Caffrey, J.M. *et al.* (2023) Contrast Enhanced Computed Tomography of Small Ruminants: Caprine and Ovine. PLOS ONE, **18**(12).
[27] Shergold, O.A., Fleck, F.A., and Radford, D. (2006) The uniaxial stress versus strain response of pig skin and silicone rubber at low and high strain rates. Int. J. Impact Eng., **32**(9)1384-1402.

[28] Gibbons, M.M., Dang, X., Adkins, M., Powell, B., and Chan, P. (2015) Finite Element Modeling of Blast Lung Injury in Sheep. *J. Biomech. Eng.,* **137**(4).
[29] Stemper, B.D., Board, D., Yoganandan, N., and Wolfla, C.E., Biomechanical properties of human thoracic spine disc segments. J. Craniovertebral Junction Spine, **1**(1):18–22.
[30] Gaur, P. *et al.* (2016) Characterisation of human diaphragm at high strain rate loading. J. Mech. Behav. Biomed. Mater., **60:**603–616.
[31] Sommer, G. *et al.* (2015) Biomechanical properties and microstructure of human ventricular myocardium. Acta Biomater., **24:**172–192.
[32] Poulard, D. and Subit, D. (2015) Unveiling the Structural Response of the Ribcage: Contribution of the Intercostal Muscles to the Thoracic Mechanical Response. ESV, **24**(15)0387.
[33] Eskandari, M., Arvayo, A.L., and Levenston, M. (2018) Mechanical properties of the airway tree: heterogeneous and anisotropic pseudoelastic and viscoelastic tissue responses. J Applied Phys, **125**(3):878-888.
[34] Eaton, M.A.K., Panzer, M.B., and Salzar, R.S. (2021) Characterizing the Response of Lung Tissue in Shear and Indentation Quasi-Static Loading. **21**(32):222-231.
[35] Comley, K. and Fleck, N. (2012) The compressive response of porcine adipose tissue from low to high strain rate. Int. J. Impact Eng., **46**:1–10.
[36] Gahagnon, S., Mofid, Y., Josse, G., and Ossant, F. (2012) Skin anisotropy in vivo and initial natural stress effect: a quantitative study using high-frequency static elastography. J. Biomech., **45**(16):2860–2865.
[37] Ní Annaidh, A., Bruyère, K., Destrade, M., Gilchrist, M.D., and Otténio, M. (2012) Characterization of the anisotropic mechanical properties of excised human skin. J. Mech. Behav. Biomed. Mater., **5**(1):139–148.
[38] Shergold, O.A., Fleck, N.A., and Radford, D. (2006) The uniaxial stress versus strain response of pig skin and silicone rubber at low and high strain rates. Int. J. Impact Eng., **32**(9)1384–1402.
[39] Gayzik, F.S, Moreno, D.P., Vavalle, N.A., Rhyne, A.C., and Stitzel, A.D. (2012) Development of a full human body finite element model for blunt injury prediction utilizing a multi-modality medical imaging protocol. *12th International LS-DYNA User Conference*, 2012, Detroit, USA.
[40] Saraf, H., Ramesh, K.T., Lennon, A.M., Merkle, A.C., and Roberts, J.C. (2007) Mechanical properties of soft human tissues under dynamic loading. J. Biomech., **40**(9):1960–1967.
[41] Untaroiu, C.D., Lu, Y.C., Siripurapu, S.K., and Kemper, A.R. (2015) Modeling the biomechanical and injury response of human liver parenchyma under tensile loading. J. Mech. Behav. Biomed. Mater., **41**:280–291.
[42] Pezowicz, C.A., Schechtman, H., Robertson, P.A., and Broom, N.D. (2006) Mechanisms of Anular Failure Resulting From Excessive Intradiscal Pressure: A Microstructural-Micromechanical Investigation. Spine, **31**(25):2891-2903.
[43] Duprey, S., Subit, D., Guillemot, H., and Kent, R.W. (2009) Biomechanical properties of the costovertebral joint. Med. Eng. Phys., **32**(2)222-227.
[44] Hodges, G. *et al.*, (2022) Ballistic loading and survivability of optical fiber sensing layers for soft body armor evaluation. Opt. Fiber Technol., **73**(103043).
[45] Goode, T., Shoemaker, G., Schultz, S., Peters, K., and Pankow, M. (2019) Soft body armor time-dependent back face deformation (BFD) with ballistics gel backing. Compos. Struct., **220:**687–698.
[46] Bass. C.R. *et al.* (2006) Injury Risk in Behind Armor Blunt Thoracic Trauma. *I*nt. J. Occup. Saf. Erg*on.*, **12**(4):429-442.
[47] Fung, Y.C., Yen, R.T., Tao, Z.L., Liu, S.Q. (1988) A hypothesis on the mechanism of trauma of lung tissue subjected to impact load. J. Biomech Eng., **110**(1):50-56.
[48] Gayzik, F.S., Hoth, J.J., Daly, M., Meredith, J.W., and Stitzel, J.D., A finite element-based injury metric for pulmonary contusion: investigation of candidate metrics through correlation with computed tomography. Stapp Car Crash J., **51**:189–209.
[49] Yuen, K., Cronin, D., and Deng, Y. (2008) Lung Response and Injury in Side Impact Conditions. IRCOBI, **8**:87-98.
[50] Gayzik, F.S. (2008) Wake Forest School of Medicine, *Development of a Finite Element Based Injury Metric for Pulmonary Contusion,* Virginia Tech Library.
[51] J. Cui, M. Rapo, K. Mathews, C. Webber, and L. Ng, "Biomechanically Based Correlate for Localized Lung Contusion From Nonlethal Blunt Impact Projectiles," *Mil. Med.*, vol. 186, no. Supplement_1, pp. 331–338, Jan. 2021, doi: 10.1093/milmed/usaa353.
[52] Miller, P.R. *et al.* (2001) ARDS after Pulmonary Contusion: Accurate Measurement of Contusion Volume Identifies High-Risk Patients. J. Trauma Acute Care Surg., **51**(2):223.
[53] Strumwasser, A., Chu, E., Yeung, L., Miraflor, E., Sadjadi, J., and Victorino, G.P. (2011) A Novel CT Volume Index Score Correlates with Outcomes in Polytrauma Patients with Pulmonary Contusion. J. Surg. Res., **170**(2):280–285.

VIII. APPENDIX

Appendix A: Model Meshing Parameters

TABLE A1
ELEMENT QUALITY CRITERIA

	Shell Elements	Solids Elements
Tet Collapse	-	0.2
Jacobian	0.4	0.3
Aspect Ratio	3.0	8.0
Skewness	60.0	70.0
Warping	30.0	50.0

TABLE A2
SHELL THICKNESS

Part	Shell Thickness (mm)
Cortical Bone	1.0
Intervertebral Discs	1.0
Diaphragm	2.5
Lung	1.0
Airway	1.0
Vasculature	1.0
Abdominal Organs	1.0
Skin	1.75

TABLE A3
THE TARGET MESH SIZE FOR THE STRUCTURES IN THE MODEL

Structure	Element Type	Target Mesh Size
Cortical Bone	Quad Shell and Tet Solid	1.0 mm
Costal Cartilage	Quad Shell and Tet Solid	1.0 mm
Lungs	Tria Shell Tet Solid	1.6 mm
Airway	Tria Shell	1.6 mm
Abdominal Organs	Tria Shell and Tet Solid	2 mm
Heart	Tria Shell and Tet Solid	1.8 mm
Vasculature	Tria Shell and Tet Solid	2.5 mm
Intervertebral Disks (IVD)	Mixed Tria and Quad Shell	1.0 mm
Intercostal Muscle (ICM)	Mixed Tet and Hex Solid	1.0 mm
Diaphragm	Mixed Tria and Quad Shell	1.6 mm
Flesh Patch and Skin	Quad Shell and Hex Solid Mesh	1.0 mm

Appendix B: The Impactor Displacement Trace for Each Impact Condition

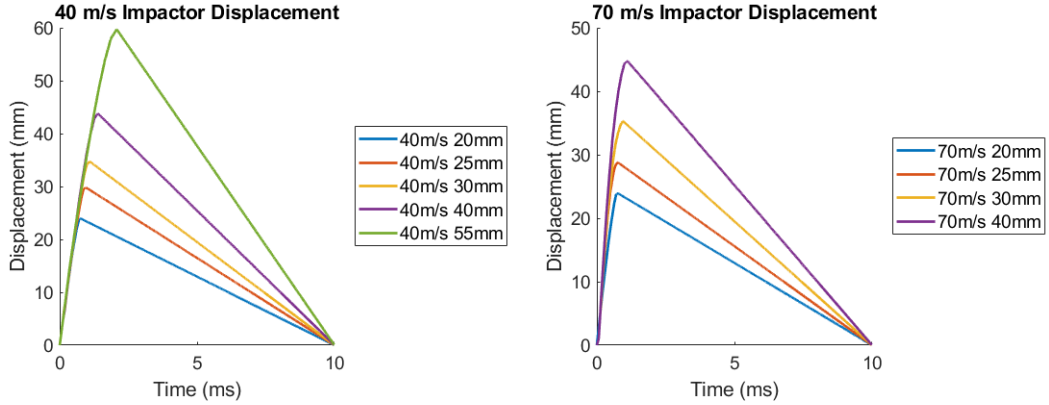

Fig B 1: Prescribed Impactor Displacement. The peak displacement of each impact curve is 5 mm higher than its displacement into the model due to the 5 mm offset of the impactor.